



## Partially embedding Pt nanoparticles in the skeleton of 3DOM $\text{Mn}_2\text{O}_3$ : An effective strategy for enhancing catalytic stability in toluene combustion

Wenbo Pei, Yuxi Liu\*, Jiguang Deng, Kunfeng Zhang, Zhiqian Hou, Xingtian Zhao, Hongxing Dai\*

*Beijing Key Laboratory for Green Catalysis and Separation, Key Laboratory of Beijing on Regional Air Pollution Control, Key Laboratory of Advanced Functional Materials, Education Ministry of China, Laboratory of Catalysis Chemistry and Nanoscience, Department of Chemistry and Chemical Engineering, College of Environmental and Energy Engineering, Beijing University of Technology, Beijing 100124, China*



### ARTICLE INFO

#### Keywords:

Three-dimensionally ordered macropore  
Manganese oxide  
Platinum embedding  
Supported noble metal catalyst  
Toluene combustion

### ABSTRACT

Polymethyl methacrylate-templating and ethylene glycol reduction methods were adopted to prepare the nanosized Pt catalysts ( $x$  wt% Pt/3DOM  $\text{Mn}_2\text{O}_3$ ;  $x = 0.2\text{--}2.3$ ) that were partially embedded in the skeleton of three-dimensionally ordered macroporous (3DOM)  $\text{Mn}_2\text{O}_3$ . These materials possessed a surface area of  $33\text{--}36 \text{ m}^2/\text{g}$ , with the Pt NPs (3.6–4.4 nm in size) being well embedded in the skeleton of 3DOM  $\text{Mn}_2\text{O}_3$ . The 2.3 wt% Pt/3DOM  $\text{Mn}_2\text{O}_3$  sample showed the best activity and the lowest apparent activation energy (41 kJ/mol) for toluene combustion, which was related to its high adsorbed oxygen species concentration and good low-temperature reducibility. Compared with 2.0 wt% Pt/3DOM  $\text{Mn}_2\text{O}_3$ -imp derived from the colloid adsorption method, 2.3 wt% Pt/3DOM  $\text{Mn}_2\text{O}_3$  exhibited a better catalytic stability within 60 h of toluene combustion. After calcination at 650 °C for 3 h, the average particle size of Pt nanoparticles (NPs) in 2.3 wt% Pt/3DOM  $\text{Mn}_2\text{O}_3$  grew up slightly from 4.3 to 4.9 nm and toluene conversions decreased slightly, while that of Pt NPs in 2.0 wt% Pt/3DOM  $\text{Mn}_2\text{O}_3$ -imp increased greatly from 4.4 to 13.7 nm and toluene conversions dropped significantly. Effects of  $\text{H}_2\text{O}$ ,  $\text{CO}_2$ , and  $\text{SO}_2$  on activity of 2.3 wt% Pt/3DOM  $\text{Mn}_2\text{O}_3$  and 2.0 wt% Pt/3DOM  $\text{Mn}_2\text{O}_3$ -imp were also examined. Partial deactivation induced by  $\text{H}_2\text{O}$  or  $\text{CO}_2$  addition was reversible, whereas that due to  $\text{SO}_2$  introduction was irreversible. It is concluded that the strong interaction between Pt NPs and 3DOM  $\text{Mn}_2\text{O}_3$  was responsible for excellent stability of the partially Pt-embedded 3DOM  $\text{Mn}_2\text{O}_3$  sample in toluene combustion.

### 1. Introduction

Most of volatile organic compounds (VOCs) are pollutants to the atmosphere and human health [1]. Due to high efficiency and low cost, catalytic oxidation has been regarded as one of the most promising pathways for VOCs removal [2,3]. Various catalysts, such as supported noble metals, transition metal oxides, and mixed oxides, have been developed for the oxidation of VOCs, among which the Pd or Pt nanoparticles (NPs) well dispersed on the surface of a high-surface-area support are the most active catalysts.

Pt NPs are highly active for the oxidation of VOCs [4]. When the supported noble metal catalysts are exposed to high temperatures (above 300 °C), however, the noble metal NPs could agglomerate to big particles, causing a decline in activity. For instance, activities of the catalysts supported Pt obviously decreased after high temperature aging treatments as a result of the sintering of Pt NPs [5]. Hence, development of durable and anti-sintering Pt catalysts is highly desirable in the

applications of VOCs elimination.

In recent years, there have been several reports on improving thermal stability of the precious metals. For instance, Xia and coworkers [6,7] designed a thermally stable catalytic system, in which Pt NPs were loaded on a  $\text{TiO}_2$  nanofiber and coated with a porous  $\text{SiO}_2$  shell (porous  $\text{SiO}_2/\text{Pt}/\text{TiO}_2$ ) and Pt NPs were embedded in the inner surface of  $\text{CeO}_2$  hollow fibers ( $\text{Pt}_{\text{encap}}/\text{CeO}_2$ ). Lu et al. [8] coated Pd NPs on the layer of alumina via an atomic layer deposition (ALD) route, and found that such a catalyst was resistant to coking in the oxidative dehydrogenation of ethane to ethylene at 650 °C and to sintering after reaction at 675 °C for 28 h. Liu et al. [9] deposited  $\text{Co}_3\text{O}_4$  on Pt NPs on the  $\text{Al}_2\text{O}_3$  support ( $\text{Co}_3\text{O}_4/\text{Pt}/\text{Al}_2\text{O}_3$ ) by the area-selective atomic layer deposition (AS-ALD) method, and observed that such a catalyst architecture exhibited excellent sintering resistance, with the high catalytic activity being maintained after the catalyst was calcined at 600 °C. The above catalysts were of a core-shell structure or coated with a highly thermally stable film. However, there has been few in situ preparation

\* Corresponding authors.

E-mail addresses: [yxliu@bjut.edu.cn](mailto:yxliu@bjut.edu.cn) (Y. Liu), [hxdai@bjut.edu.cn](mailto:hxdai@bjut.edu.cn) (H. Dai).

of noble metal NPs that were embedded in the surface of a support in the literature.

In recent years, three-dimensionally ordered macroporous (3DOM) transition metal oxide-supported noble metal NPs have been reported to show good catalytic performance due to their high surface areas and easy diffusion property. Our group previously prepared the Au/3DOM  $\text{Mn}_2\text{O}_3$ , Pd/3DOM  $\text{Mn}_2\text{O}_3$ , and AuPd/3DOM  $\text{Mn}_2\text{O}_3$  catalysts that were active for toluene combustion [10]. However, thermal stability of the 3DOM  $\text{Mn}_2\text{O}_3$ -supported Au, Pd or AuPd samples were not good enough after 60 h of on-stream toluene oxidation. Herein, we propose a new in-situ noble metal-embedded catalyst preparation strategy, in which Pt NPs were partially embedded in the skeleton of 3DOM  $\text{Mn}_2\text{O}_3$ . It is found that the Pt-embedded 3DOM  $\text{Mn}_2\text{O}_3$  samples showed excellent thermal stability in the combustion of toluene.

## 2. Experimental

### 2.1. Catalyst preparation

The Pt NPs with a particle size of approximately 1.7 nm were prepared according to the method reported in the literature [11]. Typically, an ethylene glycol (EG) solution of NaOH (20 mL, 0.26 mol/L) was added dropwise to an EG solution of  $\text{H}_2\text{PtCl}_6 \cdot 6\text{H}_2\text{O}$  (20 mL, 20 g/L) under stirring. After stirring for 30 min, and then heated at 160 °C in an oil bath for 3 h under nitrogen atmosphere, thus obtaining the dark-brown Pt colloid suspension (Pt concentration ≈ 3.7 g/L). Fig. S1 shows the TEM image of the obtained Pt NPs. Obviously, the Pt NPs were uniform and their sizes were 1–3 nm.

3DOM  $\text{Mn}_2\text{O}_3$  was synthesized via the polymethyl methacrylate (PMMA)-templating pathway described previously [10]. The Pt NPs-embedded 3DOM  $\text{Mn}_2\text{O}_3$  ( $x$  wt% Pt/3DOM  $\text{Mn}_2\text{O}_3$ ) were fabricated as follows: 20 mmol of 50 wt%  $\text{Mn}(\text{NO}_3)_2$  aqueous solution was dissolved in 6 mL of methanol (MeOH) under stirring at room temperature. The above solution was then mixed with 1, 2, 3, and 4 mL of the Pt NPs-EG solution (the theoretical Pt loadings were 0.23, 0.46, 0.69, and 0.92 wt %, respectively). The other steps were the same as those for the preparation of 3DOM  $\text{Mn}_2\text{O}_3$ . Due to the limited pore volume of the PMMA template, only a small part of  $\text{Mn}(\text{NO}_3)_2$  aqueous solution entered the interstitial voids of the well-aligned PMMA microspheres and a substantial amount of  $\text{Mn}(\text{NO}_3)_2$  aqueous solution was filtered, leading to the actual Pt loadings higher than the corresponding theoretical Pt loadings. The actual Pt loadings ( $x$ ) in the as-generated the  $x$  wt% Pt/3DOM  $\text{Mn}_2\text{O}_3$  samples were 0.2, 0.5, 1.6, and 2.3, respectively.

For comparison purposes, the 3DOM  $\text{Mn}_2\text{O}_3$ -supported Pt sample was prepared by the gas bubble-assisted colloid adsorption method. Typical, the EG solution containing the Pt NPs with a theoretical loading of 2.3 wt% was first diluted in ethanol, and then added to the 3DOM  $\text{Mn}_2\text{O}_3$  support. After bubbling the suspension with a  $\text{N}_2$  flow of 200 mL/min for 6 h, the mixture was filtered, washed with deionized water and ethanol several times, dried at 80 °C for 12 h, and calcined in an air flow of 100 mL/h at a ramp of 1 °C/min from RT to 500 °C and

maintained at this temperature for 5 h, thus obtaining the Pt/3DOM  $\text{Mn}_2\text{O}_3$  sample with an actual Pt loading of 2.0 wt% (denoted as 2.0 Pt/3DOM  $\text{Mn}_2\text{O}_3$ -imp).

### 2.2. Catalyst characterization

Physicochemical properties of the samples were characterized using the techniques, such as inductively coupled plasma atomic emission spectroscopy (ICP-AES), X-ray diffraction (XRD), scanning electron microscopy (SEM),  $\text{N}_2$  adsorption-desorption (BET), transmission electron microscopy (TEM), high angle annular dark field-scanning transmission electron microscopy (HAADF-STEM) and element mapping, energy-dispersive spectroscopy (EDS), X-ray photoelectron spectroscopy (XPS), oxygen temperature-programmed desorption ( $\text{O}_2$ -TPD), and hydrogen temperature-programmed reduction ( $\text{H}_2$ -TPR). The detailed procedures are described in the Supplementary material.

### 2.3. Catalytic evaluation

Catalytic activities for toluene oxidation of the samples were evaluated in a continuous flow fixed-bed quartz microreactor. The reactant feed was 1000 ppm toluene + 20%  $\text{O}_2$  +  $\text{N}_2$  (balance) and the space velocity (SV) was ca. 40,000 mL/(g h). The detailed evaluation procedures are stated in the Supplementary material.

## 3. Results and discussion

### 3.1. Crystal phase composition, morphology, pore structure, surface area, and Pt content

XRD patterns of the as-prepared samples are illustrated in Fig. S2(A). It can be realized that all of the diffraction signals could be indexed to the cubic  $\text{Mn}_2\text{O}_3$  phase (JCPDS PDF# 71-0636). The diffraction peaks at  $2\theta = 39.8^\circ$  and  $46.2^\circ$  (Fig. S2(B)) were due to the (111) and (200) crystal planes of the Pt phase in the 2.0 Pt/3DOM  $\text{Mn}_2\text{O}_3$ -imp and 2.3 Pt/3DOM  $\text{Mn}_2\text{O}_3$  samples, respectively, whereas no Pt phase was detected in the 0.2 Pt/3DOM  $\text{Mn}_2\text{O}_3$ , 0.5 Pt/3DOM  $\text{Mn}_2\text{O}_3$ , and 1.6 Pt/3DOM  $\text{Mn}_2\text{O}_3$  samples due to the low Pt loadings and high dispersion of Pt NPs on the surface of these samples. The grain sizes of xPt/3DOM  $\text{Mn}_2\text{O}_3$  were 31–43 nm (Table 1).

Fig. 1 shows the SEM images of the samples. Apparently, all of the samples possessed a high-quality 3DOM architecture, and the average pore sizes were in the range of 180–210 nm (Table 1). Fig. 2 shows the TEM images of the xPt/3DOM  $\text{Mn}_2\text{O}_3$  and 2.0 Pt/3DOM  $\text{Mn}_2\text{O}_3$ -imp samples. In addition to presence of a 3DOM structure, one can observe that most Pt NPs were well embedded in the skeleton of 3DOM  $\text{Mn}_2\text{O}_3$  and some Pt NPs were encapsulated by the  $\text{Mn}_2\text{O}_3$  in xPt/3DOM  $\text{Mn}_2\text{O}_3$  (Fig. 2a–f), whereas Pt NPs were dispersed on the surface of 3DOM  $\text{Mn}_2\text{O}_3$  in 2.0 Pt/3DOM  $\text{Mn}_2\text{O}_3$ -imp (Fig. 2g and h). It should be pointed out that the one-step catalyst preparation strategy adopted in the present work could not guarantee that all of the Pt NPs were embedded in

Table 1

BET surface areas, pore volumes, pore sizes, average crystallite sizes ( $D_{\text{Mn}_2\text{O}_3}$ ), average Pt particle sizes, and actual Pt loadings of the as-obtained samples.

Sample	BET surface area (m <sup>2</sup> /g)	Pore volume (cm <sup>3</sup> /g)	Macropore diameter <sup>a</sup> (nm)	$D_{\text{Mn}_2\text{O}_3}$ <sup>b</sup> (nm)	Pt particle size <sup>c</sup> (nm)	Actual Pt loading <sup>d</sup> (wt%)
3DOM $\text{Mn}_2\text{O}_3$	35.7	0.178	180–190	35	–	–
0.2 Pt/3DOM $\text{Mn}_2\text{O}_3$	34.5	0.180	170–180	32	3.6	0.2
0.5 Pt/3DOM $\text{Mn}_2\text{O}_3$	33.8	0.233	175–185	31	3.7	0.5
1.6 Pt/3DOM $\text{Mn}_2\text{O}_3$	32.5	0.177	175–185	39	3.9	1.6
2.3 Pt/3DOM $\text{Mn}_2\text{O}_3$	33.7	0.214	180–190	40	4.3	2.3
2.0 Pt/3DOM $\text{Mn}_2\text{O}_3$ -imp	34.9	0.227	180–190	43	4.4	2.0

<sup>a</sup> Data were estimated according to the SEM images.

<sup>b</sup> Data were obtained according to the Scherrer equation using the FWHM of the (222) line of  $\text{Mn}_2\text{O}_3$  in the XRD patterns.

<sup>c</sup> Data were estimated according to the TEM images.

<sup>d</sup> Data were determined by the ICP-AES technique.

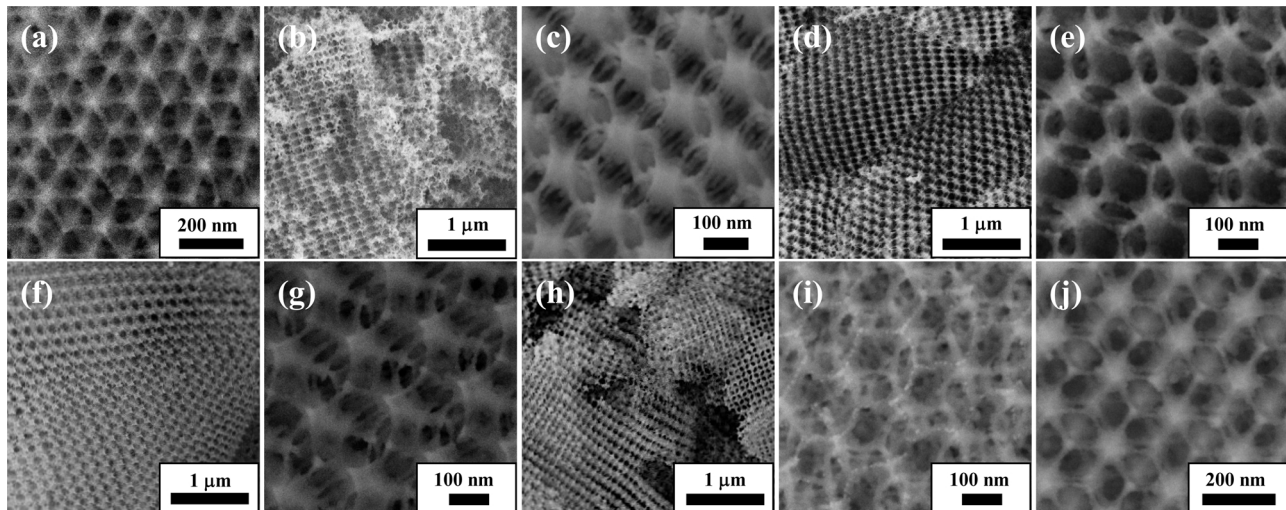


**Fig. 1.** SEM images of (a) 3DOM  $\text{Mn}_2\text{O}_3$ , (b, c) 0.2 Pt/3DOM  $\text{Mn}_2\text{O}_3$ , (d, e) 0.5 Pt/3DOM  $\text{Mn}_2\text{O}_3$ , (f, g) 1.6 Pt/3DOM  $\text{Mn}_2\text{O}_3$ , (h, i) 2.3 Pt/3DOM  $\text{Mn}_2\text{O}_3$ , and (j) 2.0 Pt/3DOM  $\text{Mn}_2\text{O}_3$ -imp.

the macropore skeleton of 3DOM  $\text{Mn}_2\text{O}_3$ . Statistical analysis of approximately 200 Pt NPs on the TEM images was performed for each sample and the average Pt particle sizes in  $x$ Pt/3DOM  $\text{Mn}_2\text{O}_3$  ( $x = 0.2, 0.5, 1.6$ , and  $2.3$ ) and 2.0/3DOM  $\text{Mn}_2\text{O}_3$ -imp were  $3.6, 3.7, 3.9, 4.3$ , and  $4.4$  nm (Fig. S3 and Table 1), respectively. As seen from the high-resolution TEM images of the samples, the interplanar spacing ( $d$  value) of  $\text{Mn}_2\text{O}_3$  was ca.  $0.28$  nm, in accordance with the (222) crystal plane of the standard  $\text{Mn}_2\text{O}_3$  material (JCPDS PDF# 71-0636); and the  $d$  value of Pt was ca.  $0.23$  nm, in accordance with the (111) crystal plane of the standard Pt sample (JCPDS PDF# 89-7382). As shown in Fig. S4, the EDS spectrum of 2.3 Pt/3DOM  $\text{Mn}_2\text{O}_3$  demonstrates existence of the Pt, Mn, and O elements in the sample. The embedding structure of Pt NPs in 2.3 Pt/3DOM  $\text{Mn}_2\text{O}_3$  was further determined using the HAADF-STEM (Fig. 3). The luminous dots in 2.3 Pt/3DOM  $\text{Mn}_2\text{O}_3$  (Fig. 3b and c) were Pt NPs that could be identified by their Pt element mapping images (Fig. 3f).

A type II isotherm with a type H3 hysteresis loop in the relative pressure ( $p/p_0$ ) range of  $0.8$ – $1.0$  and a small type H2 hysteresis loop in the  $p/p_0$  range of  $0.2$ – $0.8$  were observed from the nitrogen

adsorption–desorption isotherms of the 3DOM  $\text{Mn}_2\text{O}_3$ ,  $x$ Pt/3DOM  $\text{Mn}_2\text{O}_3$ , and 2.0 Pt/3DOM  $\text{Mn}_2\text{O}_3$ -imp samples (Fig. 4A), demonstrating existence of macropores as well as some textural mesopores within the walls of the samples [12]. The slight discrepancy of hysteresis loops in the low and high  $p/p_0$  ranges of  $x$ Pt/3DOM  $\text{Mn}_2\text{O}_3$  (or 2.0 Pt/3DOM  $\text{Mn}_2\text{O}_3$ -imp) and 3DOM  $\text{Mn}_2\text{O}_3$  indicates the difference in pore-size distribution (Fig. 4B). As summarized in Table 1, surface areas and pore volumes of these samples were in the range of  $32.5$ – $35.7$   $\text{m}^2/\text{g}$  and  $0.177$ – $0.233$   $\text{cm}^3/\text{g}$ , respectively.

It should be noted that the catalyst with a higher Pt loading would show a higher catalytic activity for toluene combustion. We tried to prepare Pt/3DOM  $\text{Mn}_2\text{O}_3$  samples with Pt loadings higher than  $2.3$  wt% using the present method. For example, we mixed 5 mL of the Pt NPs-EG solution with 6 mL of nitrate manganese precursor solution and the subsequent treatments were the same as those for the preparation of 2.3 wt% Pt/3DOM  $\text{Mn}_2\text{O}_3$ . Unfortunately, we could not obtain the  $\text{Mn}_2\text{O}_3$  with a good-quality 3DOM structure. The reason might be the viscosity of the inappropriate precursor solution (ethylene glycol concentration was too high). Considering that the 3DOM-structured

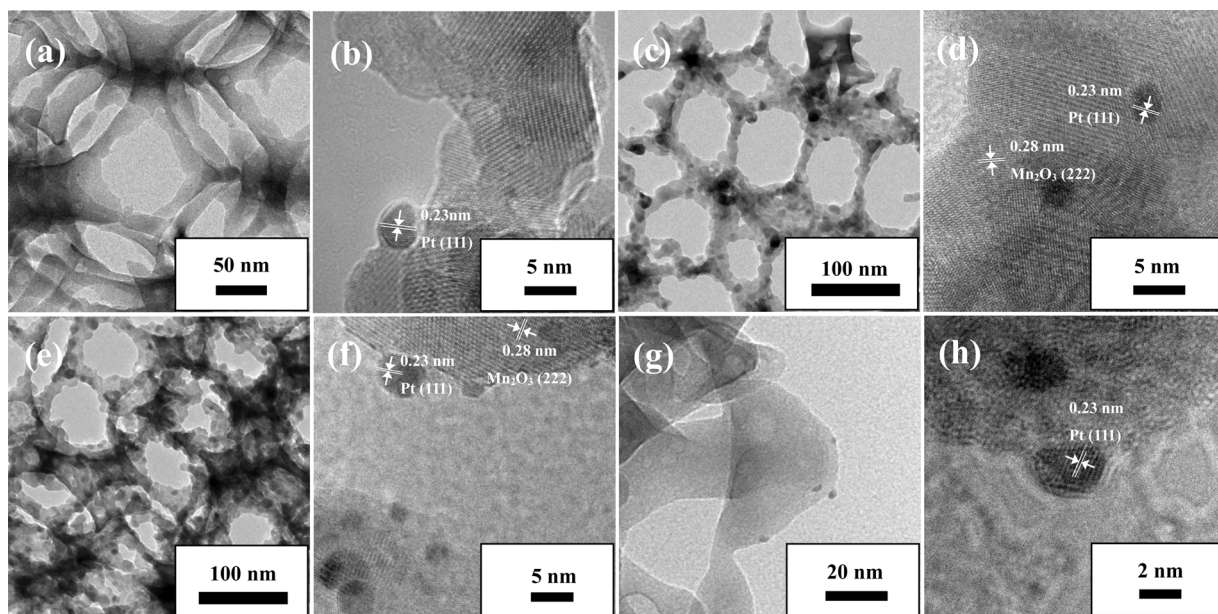


**Fig. 2.** TEM images of (a, b) 0.2 Pt/3DOM  $\text{Mn}_2\text{O}_3$ , (c, d) 0.5 Pt/3DOM  $\text{Mn}_2\text{O}_3$ , (e, f) 1.6 Pt/3DOM  $\text{Mn}_2\text{O}_3$ , (g, h) 2.0 Pt/3DOM  $\text{Mn}_2\text{O}_3$ -imp.

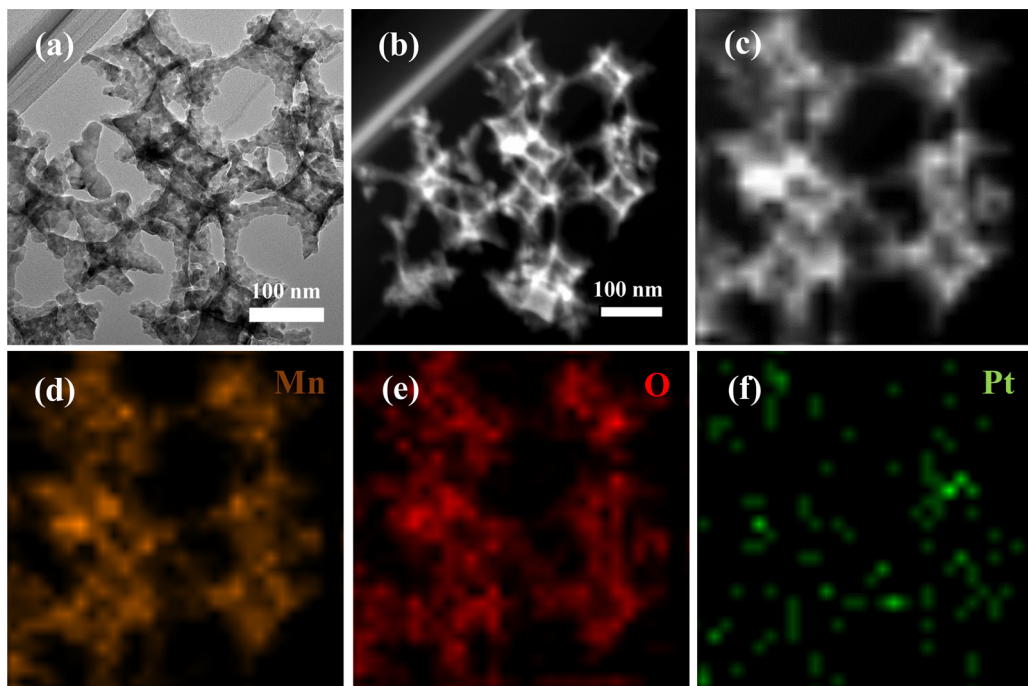


Fig. 3. (a–c) HAADF-STEM and (d–f) element mapping images of the 2.3 Pt/3DOM  $\text{Mn}_2\text{O}_3$  sample.

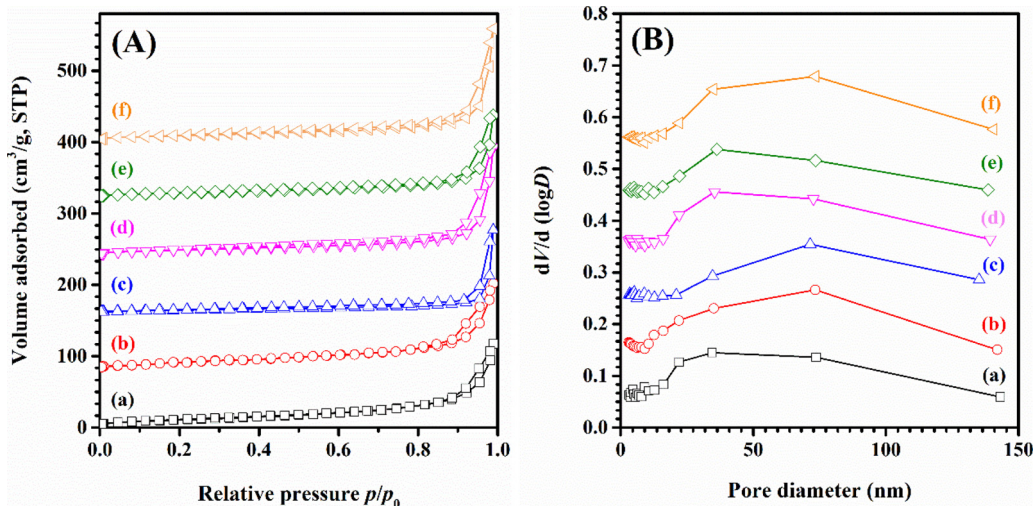


Fig. 4. (A) Nitrogen adsorption–desorption isotherms and (B) pore-size distributions of (a) 3DOM  $\text{Mn}_2\text{O}_3$ , (b) 2.0 Pt/3DOM  $\text{Mn}_2\text{O}_3$ -imp, (c) 0.2 Pt/3DOM  $\text{Mn}_2\text{O}_3$ , (d) 0.5 Pt/3DOM  $\text{Mn}_2\text{O}_3$ , (e) 1.6 Pt/3DOM  $\text{Mn}_2\text{O}_3$ , and (f) 2.3 Pt/3DOM  $\text{Mn}_2\text{O}_3$ .

samples with Pt loadings higher than 2.3 wt% were hard to be prepared using the present method and it is highly required for the Pt loadings in the supported Pt catalysts to be as low as possible for their practical applications, we did not prepare the 3DOM  $\text{Mn}_2\text{O}_3$ -supported Pt catalysts with Pt loadings higher than 2.3 wt% in the present work.

### 3.2. Surface composition, metal chemical state, and oxygen species

Fig. 5 illustrates the Mn 2p<sub>3/2</sub>, O 1s, and Pt 4f XPS spectra of the samples, and Table 2 summarizes their surface  $\text{Mn}^{3+}/\text{Mn}^{2+}$ ,  $\text{O}_{\text{ads}}/\text{O}_{\text{latt}}$ , and  $\text{Pt}^{\delta+}/\text{Pt}^0$  molar ratios. The asymmetrical Mn 2p<sub>3/2</sub> signal of each sample was decomposed into three components at BE = 640.1, 641.7, and 644.1 eV (Fig. 5A), which could be assigned to the surface  $\text{Mn}^{2+}$ ,  $\text{Mn}^{3+}$ , and  $\text{Mn}^{4+}$  species [13,14], respectively. The O 1s components of each sample at BE = 529.8, 531.3, and 533.1 eV (Fig. 5B) were ascribed to the surface lattice oxygen ( $\text{O}_{\text{latt}}$ ), adsorbed oxygen (e.g.,  $\text{O}_2^-$ ,  $\text{O}_2^{2-}$  or  $\text{O}^-$ ), and adsorbed molecular water or carbonate species [15],

respectively. As shown in Table 2, after loading of Pt NPs, the surface  $\text{Mn}^{3+}/\text{Mn}^{2+}$  molar ratio dropped from 0.87 to 0.59–0.74 (i.e., an increase in surface  $\text{Mn}^{2+}$  concentration on the sample surface). In other words, loading of Pt NPs gave rise to an increase in surface oxygen vacancy concentration of 3DOM  $\text{Mn}_2\text{O}_3$ . Furthermore, the  $\text{O}_{\text{ads}}/\text{O}_{\text{latt}}$  molar ratios (0.56–0.64) of  $x$ Pt/3DOM  $\text{Mn}_2\text{O}_3$  and 2.0 Pt/3DOM  $\text{Mn}_2\text{O}_3$ -imp were higher than that (0.46) of 3DOM  $\text{Mn}_2\text{O}_3$ . It has been reported that the electrophilic  $\text{O}_{\text{ads}}$  species played an important role in the combustion of organics [16]. A more amount of the  $\text{O}_{\text{ads}}$  species on the sample surface would favor the combustion of VOCs. As shown in Fig. 5C, the Pt 4f XPS spectrum of each sample was decomposed into six components at BE = 71.5 and 74.0 eV, 72.6 and 75.8 eV, and 74.8 and 78.1 eV that were assigned to the 4f<sub>7/2</sub> and 4f<sub>5/2</sub> orbitals of the surface metallic Pt ( $\text{Pt}^0$ ) [17],  $\text{Pt}^{2+}$  [18], and  $\text{Pt}^{4+}$  [19] species, respectively. The surface  $\text{Pt}^{\delta+}/\text{Pt}^0$  molar ratio of  $x$ Pt/3DOM  $\text{Mn}_2\text{O}_3$  increased from 1.65 to 7.16 with a rise in Pt loading from  $x$  = 0.2 to 2.3, whereas that of 2.0 Pt/3DOM  $\text{Mn}_2\text{O}_3$ -imp was 2.21.

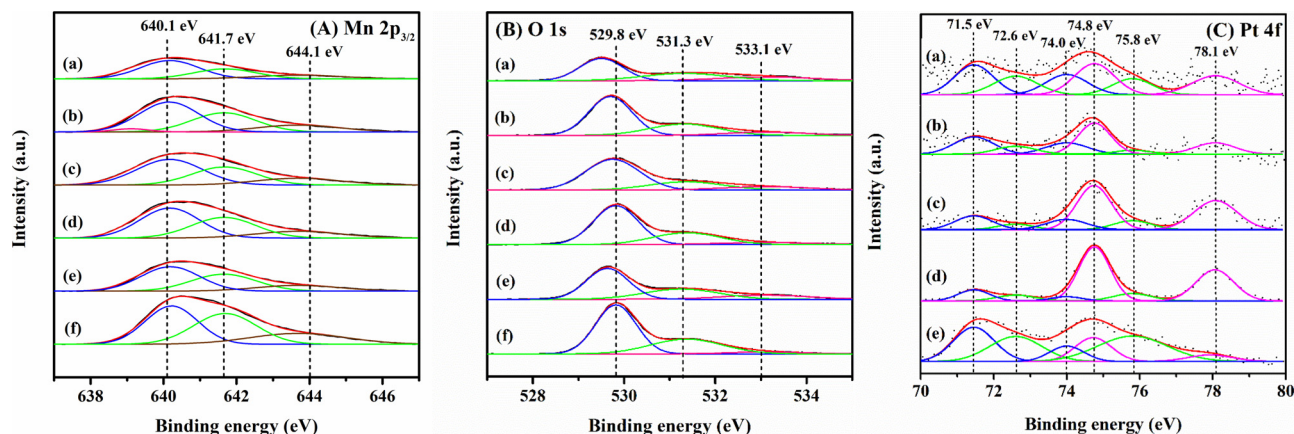


**Fig. 5.** (A) Mn 2p<sub>3/2</sub>, (B) O 1s, and (C) Pt 4f XPS spectra of (a) 0.2Pt/3DOM Mn<sub>2</sub>O<sub>3</sub>, (b) 0.5 Pt/3DOM Mn<sub>2</sub>O<sub>3</sub>, (c) 1.6 Pt/3DOM Mn<sub>2</sub>O<sub>3</sub>, (d) 2.3 Pt/3DOM Mn<sub>2</sub>O<sub>3</sub>, (e) 2.0 Pt/3DOM Mn<sub>2</sub>O<sub>3</sub>-imp, and (f) 3DOM Mn<sub>2</sub>O<sub>3</sub>.

The above results demonstrate that there was a strong metal-support interaction (SMSI) between Pt NPs and 3DOM Mn<sub>2</sub>O<sub>3</sub>. Such a SMSI might be via the electron transfer from Pt NPs to Mn<sub>2</sub>O<sub>3</sub> (Pt<sup>0</sup> + Mn<sup>3+</sup>  $\rightarrow$  Pt<sup>δ+</sup> + Mn<sup>2+</sup>). After loading of Pt NPs, the concentration of Mn<sup>3+</sup> species on the 3DOM Mn<sub>2</sub>O<sub>3</sub> surface decreased, generating the oxidized platinum (Pt<sup>2+</sup> and Pt<sup>4+</sup>) species and leading to a rise in surface Mn<sup>2+</sup> concentration (Table 2). The increase in surface Mn<sup>2+</sup> concentration induced the rise in surface oxygen vacancy density of 3DOM Mn<sub>2</sub>O<sub>3</sub>, which favored for the adsorption and activation of gas-phase oxygen to the highly active oxygen species [20].

The increase in reactive oxygen species on the surface of the samples was further confirmed by the O<sub>2</sub>-TPD profiles (Fig. 6) of 3DOM Mn<sub>2</sub>O<sub>3</sub>, 2.3 Pt/3DOM Mn<sub>2</sub>O<sub>3</sub>, and 2.0 Pt/3DOM Mn<sub>2</sub>O<sub>3</sub>-imp. There were three oxygen desorption peaks at 106, 404, and 747 °C. The former two peaks and the last peak were in line with the desorption of the O<sub>ads</sub> and O<sub>lat</sub> species [21], respectively. By quantitatively analyzing the O<sub>2</sub>-TPD profiles of the samples, one can obtain their oxygen desorption, as summarized in Table 2. Below 550 °C, oxygen desorption (0.38–0.44 mmol/g) of 2.3 Pt/3DOM Mn<sub>2</sub>O<sub>3</sub> and 2.0 Pt/3DOM Mn<sub>2</sub>O<sub>3</sub>-imp was much higher than that (0.28 mmol/g) of 3DOM Mn<sub>2</sub>O<sub>3</sub>; above 550 °C, oxygen desorption (2.10–2.51 mmol/g) of the former two samples, however, was lower than that (2.95 mmol/g) of the latter sample. These results might be owing to the interaction between Pt NPs and 3DOM Mn<sub>2</sub>O<sub>3</sub>. Such an interaction would generate a more amount of oxygen vacancies in 3DOM Mn<sub>2</sub>O<sub>3</sub>, which favored the activation of molecular oxygen to active oxygen species. The increase in surface oxygen species could promote the oxidation of VOCs (confirmed by toluene combustion activities of the samples shown below).

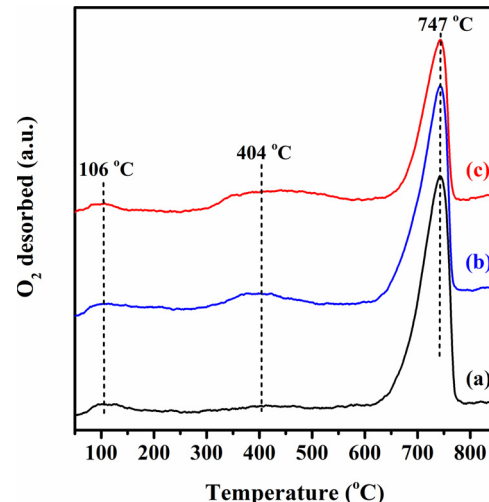


**Fig. 6.** O<sub>2</sub>-TPD profiles of (a) 3DOM Mn<sub>2</sub>O<sub>3</sub>, (b) 2.0 Pt/3DOM Mn<sub>2</sub>O<sub>3</sub>-imp, and (c) 2.3 Pt/3DOM Mn<sub>2</sub>O<sub>3</sub>.

### 3.3. Low-temperature reducibility

The reducibility of a catalyst is usually closely connected with its catalytic activity. Fig. 7 illustrates the H<sub>2</sub>-TPR profiles of the samples, and their H<sub>2</sub> consumption is also summarized in Table 2. For the 3DOM Mn<sub>2</sub>O<sub>3</sub> sample (Fig. 7A(f)), the first peak at 317 °C was assigned to reduction of Mn<sup>4+</sup> to Mn<sup>3+</sup> (Mn<sub>2</sub>O<sub>3</sub>), the second peak at 424 °C was attributed to reduction of Mn<sub>2</sub>O<sub>3</sub> to Mn<sub>3</sub>O<sub>4</sub>, and the third peak at 497 °C was ascribed to reduction of Mn<sub>3</sub>O<sub>4</sub> to MnO [22,23]. After loading of Pt NPs, the first reduction peak was shifted to lower temperatures

**Table 2**  
Surface element compositions and H<sub>2</sub> consumption of the samples.

Sample	O <sub>2</sub> desorption <sup>a</sup> (mmol/g)		Surface element composition <sup>b</sup>			H <sub>2</sub> consumption <sup>c</sup> (mmol/g)
	50–550 °C	550–850 °C	Mn <sup>3+</sup> /Mn <sup>2+</sup> molar ratio	O <sub>ads</sub> /O <sub>lat</sub> molar ratio	Pt <sup>δ+</sup> /Pt <sup>0</sup> molar ratio	
3DOM Mn <sub>2</sub> O <sub>3</sub>	0.28	2.95	0.87	0.46	–	11.42
0.2 Pt/3DOM Mn <sub>2</sub> O <sub>3</sub>	–	–	0.59	0.59	1.65	11.06
0.5 Pt/3DOM Mn <sub>2</sub> O <sub>3</sub>	–	–	0.68	0.56	1.79	10.67
1.6 Pt/3DOM Mn <sub>2</sub> O <sub>3</sub>	–	–	0.69	0.63	3.56	11.81
2.3 Pt/3DOM Mn <sub>2</sub> O <sub>3</sub>	0.38	2.10	0.74	0.64	7.16	10.98
2.0 Pt/3DOM Mn <sub>2</sub> O <sub>3</sub> -imp	0.44	2.51	0.73	0.61	2.21	10.21

<sup>a</sup> Data were calculated by quantitatively analyzing the O<sub>2</sub>-TPD profiles of the samples.

<sup>b</sup> Data were estimated by quantitatively analyzing the XPS spectra of the samples.

<sup>c</sup> Data were estimated by quantitatively analyzing the H<sub>2</sub>-TPR profiles.

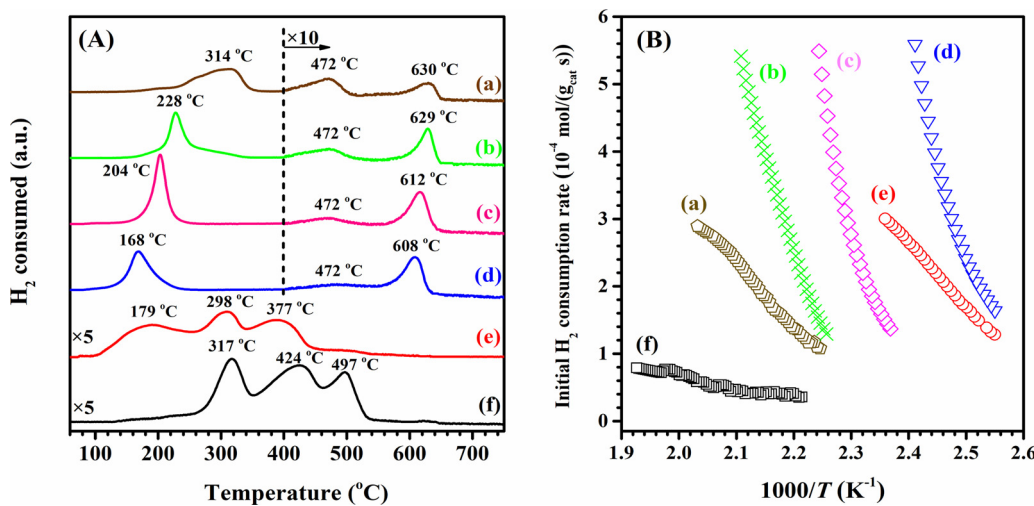


**Fig. 7.** (A) H<sub>2</sub>-TPR profiles and (B) initial H<sub>2</sub> consumption rate versus inverse temperature of (a) 0.2 Pt/3DOM Mn<sub>2</sub>O<sub>3</sub>, (b) 0.25 Pt/3DOM Mn<sub>2</sub>O<sub>3</sub>, (c) 1.6 Pt/3DOM Mn<sub>2</sub>O<sub>3</sub>, (d) 2.3 Pt/3DOM Mn<sub>2</sub>O<sub>3</sub>, (e) 2.0 Pt/3DOM Mn<sub>2</sub>O<sub>3</sub>-imp, and (f) 3DOM Mn<sub>2</sub>O<sub>3</sub>.

(168–228 °C) due to reduction of the Mn ions via the spillover of H atoms chemically adsorbed on the reduced Pt. This result demonstrates that the strong interaction between Pt NPs and 3DOM Mn<sub>2</sub>O<sub>3</sub> could enhance the low-temperature reducibility of the sample. The second and third peaks of the Pt-embedded samples (Fig. 7A(a–d)), however, were shifted to higher temperatures (472 and 608–630 °C, respectively). This result means the existence of a strong interaction between Pt NPs and lattice oxygen in the Pt-embedded samples, which would stabilize the lattice oxygen and hence cause the lattice oxygen to be more difficultly reduced by H<sub>2</sub>. However, such a strong interaction could lead to excellent thermal stability (i.e., Pt sintering was suppressed) [24]. Reduction of 2.0 Pt/3DOM Mn<sub>2</sub>O<sub>3</sub>-imp took place at 179, 298, and 377 °C (Fig. 7A(e)), which were much lower than the reduction temperatures of 3DOM Mn<sub>2</sub>O<sub>3</sub>. Based on the Mars–van Krevelen (redox) mechanism [25], one can expect that the improvement in low-temperature reducibility could enhance catalytic performance of the sample for VOCs combustion. The H<sub>2</sub> consumption (10.21–11.81 mmol/g) of xPt/3DOM Mn<sub>2</sub>O<sub>3</sub> and 2.0 Pt/3DOM Mn<sub>2</sub>O<sub>3</sub>-imp was similar to that (11.42 mmol/g) of 3DOM Mn<sub>2</sub>O<sub>3</sub>. Obviously, it can not gain useful information of reducibility from the H<sub>2</sub> consumption of the samples.

Usually, the low-temperature reducibility of a catalyst can be evaluated using the initial (where less than 25% oxygen for the first reduction peak of the sample is removed) H<sub>2</sub> consumption rate [26]. Fig. 7B shows the initial H<sub>2</sub> consumption rate as a function of inverse temperature of the samples. Apparently, the initial H<sub>2</sub> consumption rate (i.e., low-temperature reducibility) increased in the order of 3DOM Mn<sub>2</sub>O<sub>3</sub> < 0.2 Pt/3DOM Mn<sub>2</sub>O<sub>3</sub> < 0.5 Pt/3DOM Mn<sub>2</sub>O<sub>3</sub>-imp < 1.6 Pt/3DOM Mn<sub>2</sub>O<sub>3</sub> < 2.0 Pt/3DOM Mn<sub>2</sub>O<sub>3</sub>-imp < 2.3 Pt/3DOM Mn<sub>2</sub>O<sub>3</sub>, which was in good consistency with the changing trends in O<sub>ads</sub> concentration and catalytic performance (shown below).

#### 3.4. Catalytic performance

Combustion of toluene was selected to evaluate catalytic activities of the samples, as shown in Fig. 8A. We can see that the xPt/3DOM Mn<sub>2</sub>O<sub>3</sub> and 2.0 Pt/3DOM Mn<sub>2</sub>O<sub>3</sub>-imp samples performed much better than the 3DOM Mn<sub>2</sub>O<sub>3</sub> support. We use the reaction temperatures T<sub>10%</sub>, T<sub>50%</sub>, and T<sub>90%</sub> (corresponding to toluene conversion = 10, 50, and 90%) to compare catalytic activities of the samples (Table 3). The T<sub>10%</sub>, T<sub>50%</sub>, and T<sub>90%</sub> of xPt/3DOM Mn<sub>2</sub>O<sub>3</sub> and 2.0 Pt/3DOM Mn<sub>2</sub>O<sub>3</sub>-imp were much lower than those of 3DOM Mn<sub>2</sub>O<sub>3</sub>. The 2.3 Pt/3DOM Mn<sub>2</sub>O<sub>3</sub> sample performed the best: the T<sub>10%</sub>, T<sub>50%</sub>, and T<sub>90%</sub> were 135, 165, and 194 °C, respectively, which were close to those (142, 168, and

197 °C) of the 2.0 Pt/3DOM Mn<sub>2</sub>O<sub>3</sub>-imp sample. As can be seen from the HRTEM images (Fig. 2), a part of Pt NPs were encapsulated by the skeleton of Mn<sub>2</sub>O<sub>3</sub> in xPt/3DOM Mn<sub>2</sub>O<sub>3</sub> sample. Catalytic activity (T<sub>90%</sub> = 194 °C) of 2.3 Pt/3DOM Mn<sub>2</sub>O<sub>3</sub> was slightly higher than that (T<sub>90%</sub> = 197 °C) of 2.0 Pt/3DOM Mn<sub>2</sub>O<sub>3</sub>-imp (Fig. 8), in consistency with the sequence in actual Pt loading of the two samples. This result indicates that the encapsulated Pt NPs did not significantly influence catalytic activity of the sample due to the small amount of encapsulated Pt NPs by Mn<sub>2</sub>O<sub>3</sub>. Toluene combustion rates at 160 °C normalized per gram of Pt of the samples are also listed in Table 3. Apparently, toluene combustion rate (7.7 μmol/(g<sub>pt</sub> s)) of 2.3 Pt/3DOM Mn<sub>2</sub>O<sub>3</sub> was close to that (7.3 μmol/(g<sub>pt</sub> s)) of 2.0 Pt/3DOM Mn<sub>2</sub>O<sub>3</sub>-imp, but much higher than that (5.6 μmol/(g<sub>pt</sub> s)) of 0.2 Pt/3DOM Mn<sub>2</sub>O<sub>3</sub>, that (6.2 μmol/(g<sub>pt</sub> s)) of 0.5 Pt/3DOM Mn<sub>2</sub>O<sub>3</sub>, and that (6.7 μmol/(g<sub>pt</sub> s)) of 1.6 Pt/3DOM Mn<sub>2</sub>O<sub>3</sub>.

The turnover frequency (TOF<sub>pt</sub>) was calculated according to the activity data and the amounts of Pt in the samples, as listed in Table 3. The TOF<sub>pt</sub> of 0.2 Pt/3DOM Mn<sub>2</sub>O<sub>3</sub> was the highest, might due to the lowest Pt loading. The TOF<sub>pt</sub> (1.51 × 10<sup>-3</sup> s<sup>-1</sup>) of 2.3 Pt/3DOM Mn<sub>2</sub>O<sub>3</sub> was slightly higher than that (1.44 × 10<sup>-3</sup> s<sup>-1</sup>) of 2.0 Pt/3DOM Mn<sub>2</sub>O<sub>3</sub>-imp. Table S1 summarizes toluene oxidation activities of the typical samples reported in the literature. From the specific reaction rates (normalized per gram of noble metal in the sample at 160 °C) data, one can see that the specific reaction rate (7.70 μmol/(g<sub>pt</sub> s)) of 2.3 Pt/3DOM Mn<sub>2</sub>O<sub>3</sub> was much higher than that (1.14 μmol/(g<sub>pt</sub> s)) of 1.0 Pt/Al<sub>2</sub>O<sub>3</sub>–CeO<sub>2</sub> [27], that (4.54 μmol/(g<sub>pd</sub> s)) of 0.3Pd/Al<sub>2</sub>O<sub>3</sub> [28], and that (5.7 μmol/(g<sub>Au-Pd</sub> s)) of 1.99AuPd/3DOM Co<sub>3</sub>O<sub>4</sub> [29], but lower than that (34.05 μmol/(g<sub>pt</sub> s)) of 1.0 Pt–R/Beta–H [30] and that (61.91 μmol/(g<sub>pt</sub> s)) of 1.1 Pt/KBeta-SDS [31].

#### 3.5. Catalytic and thermal stability

In order to investigate stability of the catalysts, we carried out the 60-h on-stream toluene combustion over 2.3 Pt/3DOM Mn<sub>2</sub>O<sub>3</sub> at 200 °C and over 2.0 Pt/3DOM Mn<sub>2</sub>O<sub>3</sub>-imp at 180 °C and SV = 40,000 mL/(g h). It is seen from Fig. 9 that after 60 h of on-stream reaction, there was no significant drop in activity over 2.3 Pt/3DOM Mn<sub>2</sub>O<sub>3</sub>, however, a small decrease in activity (by ca. 3%) was observed over 2.0 Pt/3DOM Mn<sub>2</sub>O<sub>3</sub>-imp.

To further compare thermal stability of the Pt-embedded and Pt-supported catalysts, we calcined 2.3 Pt/3DOM Mn<sub>2</sub>O<sub>3</sub> and 2.0 Pt/3DOM Mn<sub>2</sub>O<sub>3</sub>-imp in air at 650 °C for 3 h, respectively. Fig. 10(a, c) and (b, d) shows the HAADF-STEM images of the 2.3 Pt/3DOM Mn<sub>2</sub>O<sub>3</sub> and 2.0 Pt/3DOM Mn<sub>2</sub>O<sub>3</sub>-imp samples before and after calcination at

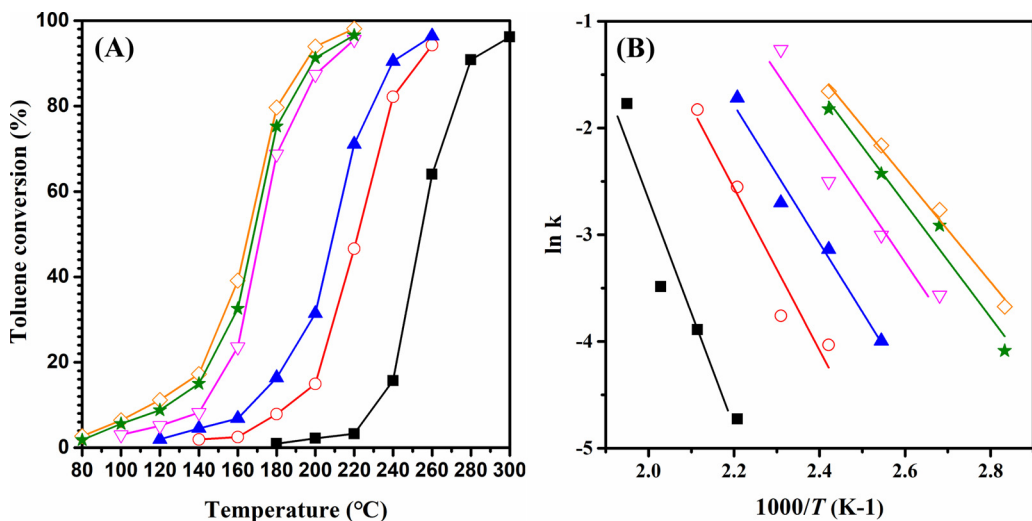


**Fig. 8.** (A) Toluene conversion and (B) Arrhenius plots as a function of reaction temperature over (■) 3DOM Mn<sub>2</sub>O<sub>3</sub>, (○) 0.2 Pt/3DOM Mn<sub>2</sub>O<sub>3</sub>, (▲) 0.5 Pt/3DOM Mn<sub>2</sub>O<sub>3</sub>, (▽) 1.6 Pt/3DOM Mn<sub>2</sub>O<sub>3</sub>, (○) 2.3 Pt/3DOM Mn<sub>2</sub>O<sub>3</sub>, and (★) 2.0 Pt/3DOM Mn<sub>2</sub>O<sub>3</sub>-imp at SV = 40,000 mL/(g h).

650 °C. It is observed that after calcination, Pt NPs in 2.3 Pt /3DOM Mn<sub>2</sub>O<sub>3</sub> were not significantly sintered, but an apparent growth of Pt NPs in 2.0 Pt/3DOM Mn<sub>2</sub>O<sub>3</sub>-imp occurred. As shown in Fig. 10e-f, average Pt particle diameter was 4.9 nm in 2.3 Pt /3DOM Mn<sub>2</sub>O<sub>3</sub>, whereas it was 13.7 nm in 2.0 Pt/3DOM Mn<sub>2</sub>O<sub>3</sub>-imp after thermal treatment at 650 °C. This result indicates that embedding Pt NPs on the skeleton of 3DOM Mn<sub>2</sub>O<sub>3</sub> could inhibit the growth of Pt NPs at high temperatures, which was due to strong interaction of Pt NPs and 3DOM Mn<sub>2</sub>O<sub>3</sub> during the encapsulation of Pt NPs in 3DOM Mn<sub>2</sub>O<sub>3</sub>. Such a strong interaction could act as an anchor that prevented the migration of Pt NPs on the manganese oxide support [32]. Moreover, it can be observed that the wall thickness of the 2.0 Pt/3DOM Mn<sub>2</sub>O<sub>3</sub>-imp sample grew up obviously after the aging treatment, and the macropores were significantly shrunk, whereas there was no obvious alteration in morphology of the 2.3 Pt/3DOM Mn<sub>2</sub>O<sub>3</sub> sample. A similar phenomenon was also reported in the literature [33]. Therefore, the strong interaction between Pt NPs and 3DOM Mn<sub>2</sub>O<sub>3</sub> not only improved catalytic stability of the sample, but also enhanced thermal stability of the 3DOM Mn<sub>2</sub>O<sub>3</sub> support. We also tested toluene combustion activity of the two samples before and after calcination, and the results are shown in Fig. 10g-h. After calcination, the activities of both samples decreased. The  $T_{50\%}$  and  $T_{90\%}$  of the 650 °C-treated 2.3 Pt/3DOM Mn<sub>2</sub>O<sub>3</sub> sample decreased by 4 and 5 °C, however, those of the 650 °C-treated 2.0 Pt/3DOM Mn<sub>2</sub>O<sub>3</sub>-imp sample dropped by 21 and 23 °C, respectively. The result demonstrates that 2.3 Pt/3DOM Mn<sub>2</sub>O<sub>3</sub> possessed better thermal stability than 2.0 Pt/3DOM Mn<sub>2</sub>O<sub>3</sub>-imp. The sintering and growth of noble metal NPs seriously affected activity of the catalyst.

Compared with the 3DOM Mn<sub>2</sub>O<sub>3</sub>-supported Pt sample, a stronger interaction between Pt and 3DOM Mn<sub>2</sub>O<sub>3</sub> was observed in the 3DOM Mn<sub>2</sub>O<sub>3</sub>-embedded Pt NPs samples, as evidenced by the shift in reduction temperature of the lattice oxygen in the H<sub>2</sub>-TPR profiles. In addition, the embedding of noble metal NPs in the skeleton of 3DOM Mn<sub>2</sub>O<sub>3</sub> could effectively inhibit sintering of the active sites, thus improving

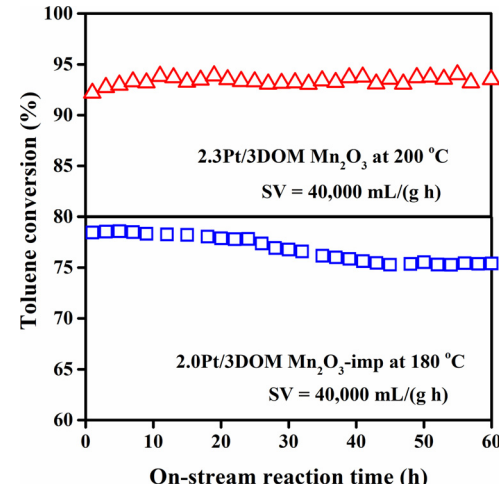


**Fig. 9.** Toluene conversion over 2.3 Pt/3DOM Mn<sub>2</sub>O<sub>3</sub> at 200 °C and 2.0 Pt/3DOM Mn<sub>2</sub>O<sub>3</sub>-imp at 180 °C within 60 h of on-stream reaction.

thermal stability of the sample. Such a result has also been confirmed by the results reported by other researchers. For instance, Flytzani-Stephanopoulos et al. [34] found that the silica-encapsulated platinum (Pt-Na@SiO<sub>2</sub>) catalysts showed remarkable stability with time-on-stream water-gas shift reaction at 350 °C. Wang et al. [35] reported that the noble metal nanocrystals (Pd nanocubes, Au nanorods, and Au core/Pd shell nanorods)-embedded hollow mesoporous TiO<sub>2</sub> and ZrO<sub>2</sub> microspheres exhibited much better catalytic activities than the commercial Pd/C catalyst for the reduction of 4-nitrophenol, and the authors thought that the noble metal nanocrystal-embedded structures could prevent aggregation of the metal nanocrystals and reduce the loss of the catalyst after recycling tests. Schüth et al. [36] prepared the Pt

**Table 3**  
Catalytic activities, TOFs, reaction rates, pre-exponential factor (A), and apparent activation energies ( $E_a$ ) at SV = 40,000 mL/(g h) of the samples.

Sample	Catalytic activity			Toluene combustion at 160 °C		A	$E_a$ (kJ/mol)
	$T_{10\%}$ (°C)	$T_{50\%}$ (°C)	$T_{90\%}$ (°C)	TOF <sub>Pt</sub> ( $\times 10^{-3}$ s <sup>-1</sup> )	Reaction rate ( $\mu\text{mol}/(\text{g}_{\text{Pt}} \text{s})$ )		
3DOM Mn <sub>2</sub> O <sub>3</sub>	233	254	280	–	–	$1.3 \times 10^8$	89
0.2 Pt/3DOM Mn <sub>2</sub> O <sub>3</sub>	184	202	253	1.09	5.6	$1.4 \times 10^6$	63
0.5 Pt/3DOM Mn <sub>2</sub> O <sub>3</sub>	177	208	240	1.21	6.2	$2.4 \times 10^5$	53
1.6 Pt/3DOM Mn <sub>2</sub> O <sub>3</sub>	145	172	206	1.30	6.7	$1.9 \times 10^5$	49
2.3 Pt/3DOM Mn <sub>2</sub> O <sub>3</sub>	135	165	194	1.51	7.7	$2.7 \times 10^4$	41
2.0 Pt/3DOM Mn <sub>2</sub> O <sub>3</sub> -imp	142	168	197	1.44	7.3	$7.2 \times 10^4$	44

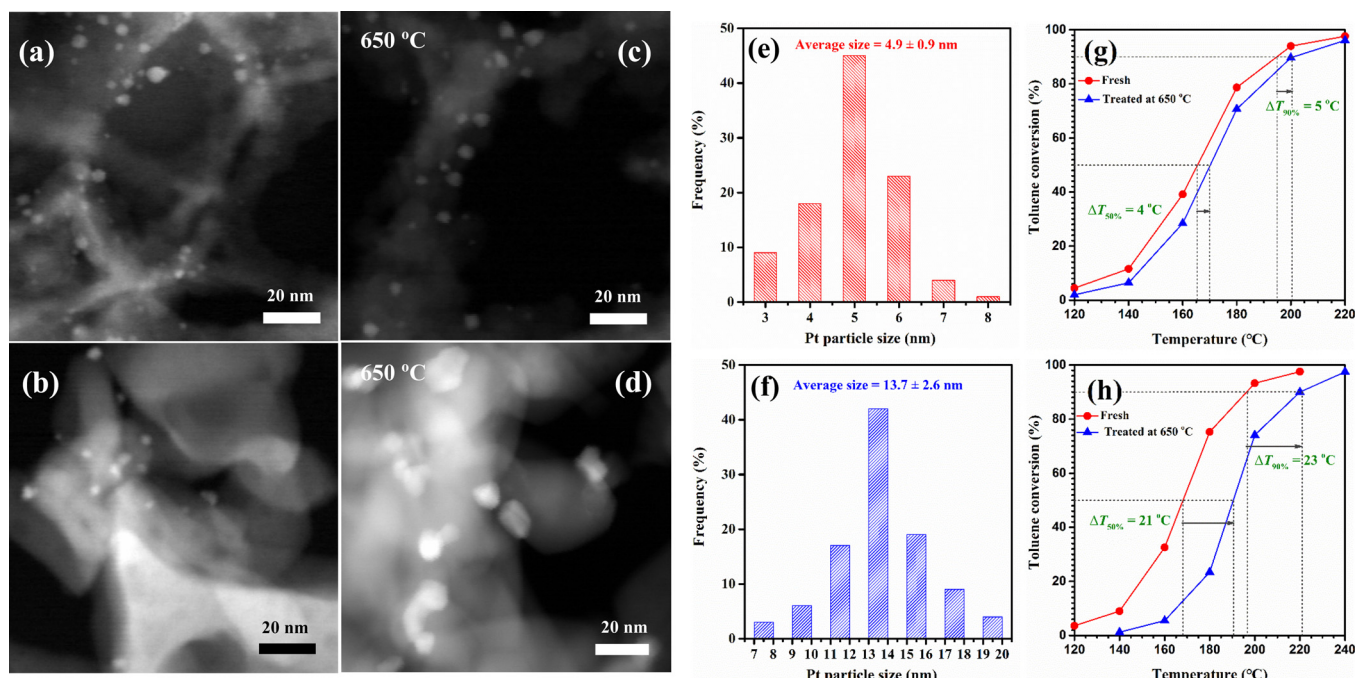


**Fig. 10.** (a–d) HAADF-STEM images, (e, f) Pt particle size distributions, and (g, h) catalytic activities of (a, c, e, g) 2.3 Pt /3DOM Mn<sub>2</sub>O<sub>3</sub> and (b, d, f, h) 2.0 Pt/3DOM Mn<sub>2</sub>O<sub>3</sub>-imp before and after calcination treatments in air at 650 °C.

NPs embedded in nitrogen-doped hollow carbon sphere (Pt@NHCS) electrocatalysts, and found that the Pt particle sizes did not change significantly after the thermal treatment at 850 °C.

### 3.6. Effects of water vapor, carbon dioxide, and sulfur dioxide

In order to examine the effect of water vapor on activity of the 2.3 Pt/3DOM Mn<sub>2</sub>O<sub>3</sub> and 2.0 Pt/3DOM Mn<sub>2</sub>O<sub>3</sub>-imp samples, we carried out toluene combustion in the presence of 3.0 or 5.0 vol% water vapor (Fig. 11A). It is found that addition of water vapor decreased toluene conversion at 195 °C, and the effect of 5.0 vol% H<sub>2</sub>O vapor was more significant than that of 3.0 vol% H<sub>2</sub>O vapor. Toluene conversion over 2.3 Pt/3DOM Mn<sub>2</sub>O<sub>3</sub> or 2.0 Pt/3DOM Mn<sub>2</sub>O<sub>3</sub>-imp decreased by 8–9% owing to the competitive adsorption of H<sub>2</sub>O. When water vapor was cut off, toluene conversion was almost restored to the initial value in the

absence of water vapor. A similar phenomenon was also observed previously [15]. As for the effect of CO<sub>2</sub> on catalytic performance, we introduced 3 vol% CO<sub>2</sub> in the feedstock at 185 °C and SV = 40,000 mL/(g h). As shown in Fig. 11B, after CO<sub>2</sub> addition, toluene conversion over 2.3 Pt/3DOM Mn<sub>2</sub>O<sub>3</sub> and 2.0 Pt/3DOM Mn<sub>2</sub>O<sub>3</sub>-imp decreased by ca. 6 and 13%, respectively. After the used samples were activated in an O<sub>2</sub> flow of 30 mL/min at 500 °C for 1 h, toluene conversion was totally recovered. Introduction of CO<sub>2</sub> brought a negative effect on activity, since the surface active sites of the samples were gradually covered by the carbonate species (formed during the combustion process) that could inhibit the activation adsorption of oxygen and/or toluene molecules [37]. After activation, the generated carbonate species decomposed completely, hence giving rise to recovering of the surface active sites. These results demonstrate that the Pt-embedded 3DOM Mn<sub>2</sub>O<sub>3</sub> sample possessed a better CO<sub>2</sub>-resistant ability, which might be due to

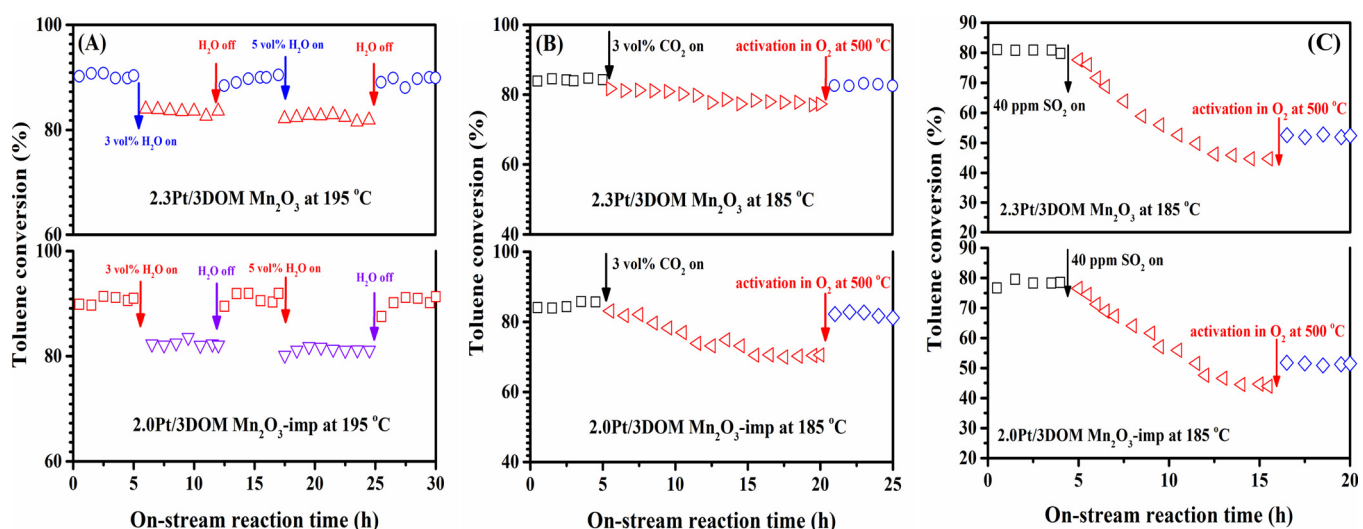


**Fig. 11.** (A) Effect of (A) H<sub>2</sub>O, (B) CO<sub>2</sub>, and (C) SO<sub>2</sub> on catalytic activity of 2.3 Pt/3DOM Mn<sub>2</sub>O<sub>3</sub> and 2.0 Pt/3DOM Mn<sub>2</sub>O<sub>3</sub>-imp at 195 or 185 °C and SV = 40,000 mL/(g h).

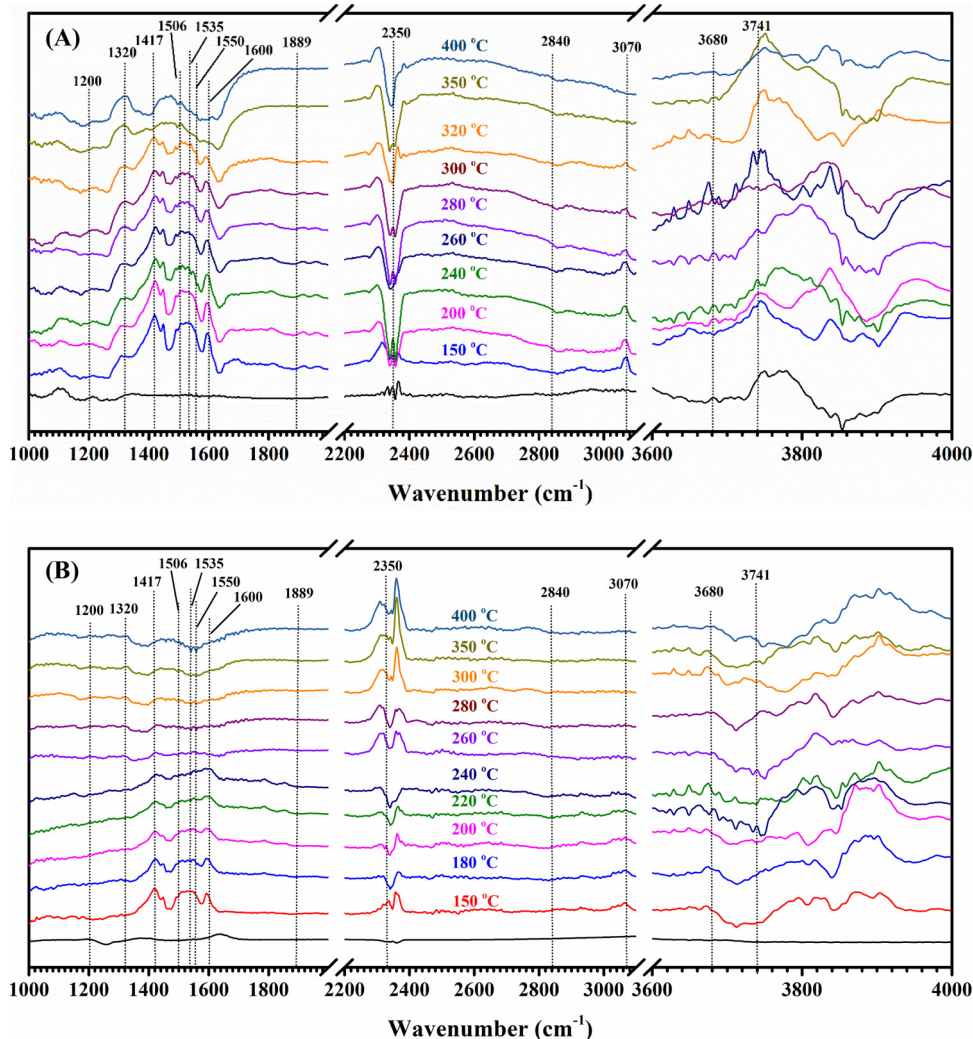


**Fig. 12.** In situ DRIFT spectra of (A) 3DOM  $\text{Mn}_2\text{O}_3$  and (B) 2.3 Pt/3DOM  $\text{Mn}_2\text{O}_3$  during toluene combustion at different temperatures (reaction conditions: 1000 ppm toluene + 20 vol%  $\text{O}_2$  +  $\text{N}_2$  (balance); SV = 40,000 mL/(g h)).

existence of a stronger interaction between Pt NPs and 3DOM  $\text{Mn}_2\text{O}_3$  of this sample.

Toluene combustion was carried out in the presence of 40 ppm  $\text{SO}_2$  in the feedstock over 2.3 Pt/3DOM  $\text{Mn}_2\text{O}_3$  and 2.0 Pt/3DOM  $\text{Mn}_2\text{O}_3$ -imp at 185 °C and SV = 40,000 mL/(g h). It is observed from Fig. 11C that toluene conversion slowly declined from ca. 81 to 45% over 2.3 Pt/3DOM  $\text{Mn}_2\text{O}_3$  and from ca. 80 to 44% over 2.0 Pt/3DOM  $\text{Mn}_2\text{O}_3$ -imp after 12 h of on-stream reaction. When the partially deactivated samples were treated in an  $\text{O}_2$  flow of 30 mL/min at 500 °C for 1 h, however, toluene conversion was not recovered. The result indicates that the partial deactivation induced by  $\text{SO}_2$  addition was irreversible. To explore the reason for such a deactivation, we recorded the FT-IR spectra of the fresh and  $\text{SO}_2$ -treated samples, as shown in Fig. S6. A broad and weak absorption band at 1135  $\text{cm}^{-1}$  assignable to the  $\text{SO}_3^{2-}$  or  $\text{SO}_4^{2-}$  species in 2.3 Pt/3DOM  $\text{Mn}_2\text{O}_3$  (Fig. S6(b)) and 2.0 Pt/3DOM  $\text{Mn}_2\text{O}_3$ -imp (Fig. S6(d)) were recorded after  $\text{SO}_2$  poisoning and activation treatments [38]. The generation of sulfate species explained the irreversible deactivation of the two samples.

### 3.7. Kinetic parameter and reaction pathway

In the past years, there have been a lot of research works related to the kinetics of catalytic VOCs oxidation. For example, Behar et al. claimed that toluene combustion over  $\text{Cu}_{1.5}\text{Mn}_{1.5}\text{O}_4$  was first- and zero-order with respect to toluene and oxygen concentrations [39],

respectively. Chen et al. found that  $\text{CH}_2\text{Cl}_2$  oxidation over  $\text{Au/Co}_3\text{O}_4$  was first- and zero-order toward  $\text{CH}_2\text{Cl}_2$  and  $\text{O}_2$  concentrations [40], respectively. In one of our previous works [41], a similar reaction mechanism was also confirmed over the Pd/meso-CoO and Pd/meso- $\text{Co}_3\text{O}_4$  catalysts. Hence, it can be reasonably assumed that toluene combustion in an excess oxygen (toluene/ $\text{O}_2$  molar ratio = 1/400) atmosphere obeys a first-order reaction mechanism with respect to toluene concentration ( $c$ ):  $r = -kc = (-A\exp(-E_a/RT))c$ , where  $r$ ,  $k$ ,  $A$ , and  $E_a$  are the reaction rate (mol/s), rate constant ( $\text{s}^{-1}$ ), pre-exponential factor, and apparent activation energy (kJ/mol), respectively.

Fig. 8B shows the Arrhenius plots for toluene combustion over xPt/3DOM  $\text{Mn}_2\text{O}_3$  and 2.0 Pt/3DOM  $\text{Mn}_2\text{O}_3$ -imp at SV = 40,000 mL/(g h), and the calculated  $A$  and  $E_a$  are summarized in Table 3. It was reported that the  $A$  value reflected the density of the active sites [42]. With the rise in Pt loading, the density of active sites increased but the  $E_a$  decreased, giving rise to a better catalytic efficiency. The lowest  $E_a$  (41 kJ/mol) was achieved over the 2.3 Pt/3DOM  $\text{Mn}_2\text{O}_3$  catalyst. By comparing with other supported noble metal catalysts (Table S1), the  $E_a$  over 2.3 Pt/3DOM  $\text{Mn}_2\text{O}_3$  was much lower than that (79 kJ/mol) over Pt@meso- $\text{Cr}_2\text{O}_3$  [43], that (104 kJ/mol) over 1.0 Pt/HPMOR [44], and that (110 kJ/mol) over 3.42 Pt-CoAlO [45], equal to that (41 kJ/mol) over Pt-R/Beta-H [30], but higher than that (36 kJ/mol) over 3.26Pd-CoAlO-Al [46], that (26 kJ/mol) over 3.8AuPd<sub>1.92</sub>/3DOM  $\text{Mn}_2\text{O}_3$  [10], and that (33 kJ/mol) over 1.99AuPd/3DOM  $\text{Co}_3\text{O}_4$  [29].

To probe the possible pathways of toluene combustion, we recorded

the in-situ DRIFT spectra (Fig. 12) of the 3DOM  $\text{Mn}_2\text{O}_3$  and 2.3 Pt/3DOM  $\text{Mn}_2\text{O}_3$  samples in the presence of 1000 ppm toluene + 20 vol%  $\text{O}_2 + \text{N}_2$  (balance) at different temperatures, and their absorption band assignments are listed in Table S2. There were characteristic peaks at 1506 and 1600  $\text{cm}^{-1}$  corresponding to the in- and out-plane deformation vibrations of benzene ring in toluene [47]. The surface OH group of the sample interacting with the methyl group of toluene at 3741 and 3680  $\text{cm}^{-1}$  and the stretching vibration of C–H bonds at 3070  $\text{cm}^{-1}$  also confirm the adsorption of toluene on the sample surface [48]. The peak intensity of toluene gradually weakened as a rise in temperature, and it was the weakest on 3DOM  $\text{Mn}_2\text{O}_3$  at 350  $^\circ\text{C}$  and on 2.3 Pt/3DOM  $\text{Mn}_2\text{O}_3$  at 260  $^\circ\text{C}$ . Meanwhile, the amounts of  $\text{CO}_2$  (at 2350  $\text{cm}^{-1}$ ) and  $\text{H}_2\text{O}$  (at 3741 and 3680  $\text{cm}^{-1}$ ) increased with temperature rise [47]. The recording of the absorption bands at 1320  $\text{cm}^{-1}$  (due to the  $\text{CH}_2$  deformation vibration of benzyl species) and 1200  $\text{cm}^{-1}$  (assignable to the C–O stretching vibration) indicates formation of benzyl alcohol [49]. Several intermediates, such as benzoic acid (1417, 1535, and 1550  $\text{cm}^{-1}$ ), benzaldehyde (2840  $\text{cm}^{-1}$ ), maleic anhydride (1889  $\text{cm}^{-1}$ ), were also detected. Based on the above in-situ DRIFT spectra and the results reported in the literature [47–49], we deduce that the gas-phase toluene was first adsorbed on the sample surface, and then partly oxidized by the active oxygen adspecies to benzyl alcohol that was subsequently transformed into benzoic acid and benzaldehyde. With a rise in temperature, the benzene ring of toluene was opened to form maleic anhydride, and finally oxidized to  $\text{CO}_2$  and  $\text{H}_2\text{O}$ .

#### 4. Conclusions

The 3DOM  $\text{Mn}_2\text{O}_3$  and partially Pt-embedded 3DOM  $\text{Mn}_2\text{O}_3$  samples with surface areas of 33–36  $\text{m}^2/\text{g}$  were prepared using the PMMA-templating and EG reduction methods, respectively. The Pt NPs displayed an average size of 3.6–4.4 nm and were well embedded in the skeleton of 3DOM  $\text{Mn}_2\text{O}_3$ . The 2.3 Pt/3DOM  $\text{Mn}_2\text{O}_3$  sample showed the best catalytic performance, together with the lowest apparent activation energy (41  $\text{kJ/mol}$ ), which was related to its higher adsorbed oxygen species concentration and better low-temperature reducibility. Compared to the 2.0 Pt/3DOM  $\text{Mn}_2\text{O}_3$ -imp sample, the 2.3 Pt/3DOM  $\text{Mn}_2\text{O}_3$  sample exhibited better catalytic stability within 60 h of on-stream reaction. After calcination at 650  $^\circ\text{C}$  for 3 h, the average particle size of Pt NPs in 2.3 Pt/3DOM  $\text{Mn}_2\text{O}_3$  grew up slightly from 4.3 to 4.9 nm and toluene conversion decreased slightly ( $\Delta T_{90\%} = 5^\circ\text{C}$ ), whereas the average particle size of Pt NPs in 2.0 Pt/3DOM  $\text{Mn}_2\text{O}_3$ -imp increased considerably from 4.4 to 13.7 nm and toluene conversion decreased greatly ( $\Delta T_{90\%} = 23^\circ\text{C}$ ). The partial deactivation induced by  $\text{H}_2\text{O}$  or  $\text{CO}_2$  addition of the 2.3 Pt/3DOM  $\text{Mn}_2\text{O}_3$  and 2.0 Pt/3DOM  $\text{Mn}_2\text{O}_3$ -imp samples was reversible, whereas that due to  $\text{SO}_2$  introduction was irreversible. It is concluded that the excellent stability of the partially Pt-embedded 3DOM  $\text{Mn}_2\text{O}_3$  sample was associated with the strong interaction between Pt NPs and 3DOM  $\text{Mn}_2\text{O}_3$ .

#### Acknowledgements

This work was supported by the NSF of China (21677004, 21876006, 21607005, and 21622701) and National Key R&D Program of China (2016YFC0204800).

#### Appendix A. Supplementary data

Supplementary material related to this article can be found, in the online version, at doi:<https://doi.org/10.1016/j.apcatb.2019.117814>.

#### References

- A.L. Bolden, C.F. Kwiatkowski, T. Colborn, New look at BTEX: are ambient levels a problem? *Environ. Sci. Technol.* 49 (2015) 5261–5276.
- Y.F. Wang, C.B. Zhang, F.D. Liu, H. He, Well-dispersed palladium supported on ordered mesoporous  $\text{Co}_3\text{O}_4$  for catalytic oxidation of o-xylene, *Appl. Catal. B* 142–143 (2013) 72–79.
- J.G. Deng, S.N. He, S.H. Xie, H.G. Yang, Y.X. Liu, G.S. Guo, H.X. Dai, Ultralow loading of silver nanoparticles on  $\text{Mn}_2\text{O}_3$  nanowires derived with molten salts: a high-efficiency catalyst for the oxidative removal of toluene, *Environ. Sci. Technol.* 49 (2015) 11089–11095.
- H.G. Yang, J.G. Deng, Y.X. Liu, S.H. Xie, Z.X. Wu, H.X. Dai, Preparation and catalytic performance of Ag, Au, Pd or Pt nanoparticles supported on 3DOM  $\text{CeO}_2\text{-Al}_2\text{O}_3$  for toluene oxidation, *J. Mol. Catal. A* 414 (2016) 9–18.
- P.J.F. Harris, The sintering of platinum particles in an alumina-supported catalyst: further transmission electron microscopy studies, *J. Catal.* 97 (1986) 527–542.
- Y.Q. Dai, B. Lim, Y. Yang, C.M. Cobley, W.Y. Li, E.C. Cho, B. Grayson, P.T. Fanson, C.T. Campbell, Y.M. Sun, Y.N. Xia, A sinter-resistant catalytic system based on platinum nanoparticles supported on  $\text{TiO}_2$  nanofibers and covered by porous silica, *Angew. Chem.* 122 (2010) 8341–8344.
- K. Yoon, Y. Yang, P. Lu, D.H. Wan, H.C. Peng, K.S. Masias, P.T. Fanson, C.T. Campbell, Y.N. Xia, A highly reactive and sinter-resistant catalytic system based on platinum nanoparticles embedded in the inner surfaces of  $\text{CeO}_2$  hollow fibers, *Angew. Chem. Int. Ed.* 51 (2012) 9543–9546.
- J.L. Lu, B.S. Fu, M.C. Kung, G.M. Xiao, J.W. Elam, H.H. Kung, P.C. Stair, Coking- and sintering-resistant palladium catalysts achieved through atomic layer deposition, *Science* 335 (2012) 1205–1208.
- X. Liu, Q.Q. Zhu, Y. Lang, K. Cao, S.Q. Chu, B. Shan, R. Chen, Oxide-nanotrap-anchored platinum nanoparticles with high activity and sintering resistance by area-selective atomic layer deposition, *Angew. Chem.* 129 (2017) 1670–1674.
- S.H. Xie, J.G. Deng, Y.X. Liu, Z.H. Zhang, H.G. Yang, Y. Jiang, H. Arandiyan, H.X. Dai, C.T. Au, Excellent catalytic performance, thermal stability, and water resistance of 3DOM  $\text{Mn}_2\text{O}_3$ -supported Au–Pd alloy nanoparticles for the complete oxidation of toluene, *Appl. Catal. A* 507 (2015) 82–90.
- C. Lian, H.Q. Liu, C. Xiao, W. Yang, K. Zhang, Y. Liu, Y. Wang, Solvent-free selective hydrogenation of chloronitrobenzene to chloroaniline over a robust  $\text{Pt/Fe}_3\text{O}_4$  catalyst, *Chem. Commun.* 48 (2012) 3124–3126.
- X.W. Li, H.X. Dai, J.G. Deng, Y.X. Liu, S.H. Xie, Z.X. Zhao, Y. Wang, H. Arandiyan, Au/3DOM  $\text{LaCoO}_3$ : high-performance catalysts for the oxidation of carbon monoxide and toluene, *Chem. Eng. J.* 228 (2013) 965–975.
- T.K. Tseng, H. Chu, H.H. Hsu, Characterization of  $\gamma$ -alumina-supported manganese oxide as an incineration catalyst for trichloroethylene, *Environ. Sci. Technol.* 37 (2003) 171–176.
- D.S. Zhang, L. Zhang, L.Y. Shi, C. Fang, H.R. Li, R.H. Gao, L. Huang, J.P. Zhang, In situ supported  $\text{Mn}_{0.8}\text{-CeO}_x$  on carbon nanotubes for the low-temperature selective catalytic reduction of NO with  $\text{NH}_3$ , *Nanoscale* 5 (2013) 1127–1136.
- Y.C. Wei, J. Liu, Z. Zhao, Y.S. Chen, C.M. Xu, A.J. Duan, G.Y. Jiang, H. He, Highly active catalysts of gold nanoparticles supported on three-dimensionally ordered macroporous  $\text{LaFeO}_3$  for soot oxidation, *Angew. Chem. Int. Ed.* 50 (2011) 2326–2329.
- S. Rousseau, S. Lordin, P. Delichere, A. Boreave, J.P. Deloume, P. Vernoux,  $\text{La}_{(1-x)}\text{Sr}_x\text{Co}_{1-y}\text{Fe}_y\text{O}_3$  perovskites prepared by sol-gel method: characterization and relationships with catalytic properties for total oxidation of toluene, *Appl. Catal. B* 88 (2009) 438–447.
- Y.B. He, G.R. Li, Z.L. Wang, Y.N. Ou, Y.X. Tong, Pt nanorods aggregates with enhanced electrocatalytic activity toward methanol oxidation, *J. Phys. Chem. C* 114 (2010) 19175–19181.
- J. Prabhuram, T.S. Zhao, C.W. Wong, J.W. Guo, Synthesis and physical/electrochemical characterization of Pt/C nanocatalyst for polymer electrolyte fuel cells, *J. Power Sources* 134 (2004) 1–6.
- X. Cheng, Y.H. Li, L.R. Zheng, Y. Yan, Y.F. Zhang, G. Chen, S.R. Sun, J.J. Zhang, Highly active, stable oxidized platinum clusters as electrocatalysts for the hydrogen evolution reaction, *Energy Environ. Sci.* 10 (2017) 2450–2458.
- M.M. Schubert, S. Hackenberg, A.C.V. Veen, M. Muhler, V. Plzak, R.J. Behm, CO oxidation over supported gold catalysts – “inert” and “active” support materials and their role for the oxygen supply during reaction, *J. Catal.* 197 (2001) 113–122.
- P. Li, C. He, J. Cheng, C.Y. Ma, B.J. Dou, Z.P. Hao, Catalytic oxidation of toluene over  $\text{Pd/Co}_3\text{AlO}$  catalysts derived from hydrotalcite-like compounds: effects of preparation methods, *Appl. Catal. B* 101 (2011) 570–579.
- W.X. Tang, X.F. Wu, D.Y. Li, Z. Wang, G. Liu, H.D. Liu, Y.F. Chen, Oxalate route for promoting activity of manganese oxide catalysts in total VOCs’ oxidation: effect of calcination temperature and preparation method, *J. Mater. Chem. A* 2 (2014) 2544–2554.
- S.C. Kim, W.G. Shim, Catalytic combustion of VOCs over a series of manganese oxide catalysts, *Appl. Catal. B* 98 (2010) 180–185.
- L. Nie, D.H. Mei, H.F. Xiong, B. Peng, Z.B. Ren, X.I.P. Hernandez, A. DeLaRiva, M. Wang, M.H. Engelhard, L. Kovarik, A.K. Datye, Y. Wang, Activation of surface lattice oxygen in single-atom Pt/ $\text{CeO}_2$  for low-temperature CO oxidation, *Science* 358 (2017) 1419–1423.
- B.C. Liu, Y. Liu, C.Y. Li, W.T. Hua, P. Jing, Q. Wang, Three-dimensionally ordered macroporous Au/ $\text{CeO}_2\text{-Co}_3\text{O}_4$  catalysts with nanoporous walls for enhanced catalytic oxidation of formaldehyde, *J. Appl. Catal. B* 127 (2012) 47–58.
- K.D. Chen, S.B. Xie, A.T. Bell, E. Iglesia, Structure and properties of oxidative dehydrogenation catalysts based on  $\text{MoO}_3\text{/Al}_2\text{O}_3$ , *J. Catal.* 198 (2001) 232–242.
- Z. Abbas, M. Haghghi, E. Fatehifar, S. Saedy, Synthesis and physicochemical characterizations of nanostructured  $\text{Pt/Al}_2\text{O}_3\text{-CeO}_2$  catalysts for total oxidation of VOCs, *J. Hazard. Mater.* 186 (2011) 1445–1454.
- W.G. Shim, J.W. Lee, S.C. Kim, Analysis of catalytic oxidation of aromatic hydrocarbons over supported palladium catalyst with different pretreatments based on heterogeneous adsorption properties, *Appl. Catal. B* 84 (2008) 133–141.
- S.H. Xie, J.G. Deng, S.M. Zang, H.G. Yang, G.S. Guo, H. Arandiyan, H.X. Dai,

Au–Pd/3DOM  $\text{Co}_3\text{O}_4$ : highly active and stable nanocatalysts for toluene oxidation, *J. Catal.* 322 (2015) 38–48.

[30] C.Y. Chen, J. Zhu, F. Chen, X.J. Meng, X.M. Zheng, X.H. Gao, F.S. Xiao, Enhanced performance in catalytic combustion of toluene over mesoporous Beta zeolite-supported platinum catalyst, *Appl. Catal. B* 140–141 (2013) 199–205.

[31] C.Y. Chen, Q.M. Wu, F. Chen, L. Zhang, S.X. Pan, C.Q. Bian, X.M. Zheng, X.J. Meng, F.S. Xiao, Aluminium-rich Beta zeolite-supported platinum nanoparticles for the low-temperature catalytic removal of toluene, *J. Mater. Chem. A* 3 (2015) 5556–5562.

[32] Y. Nagai, T. Hirabayashi, K. Dohmaea, N. Takagi, T. Minami, H. Shinjoh, S. Matsumoto, Sintering inhibition mechanism of platinum supported on ceria-based oxide and Pt-oxide–support interaction, *J. Catal.* 242 (2006) 103–109.

[33] J. Lee, Y.S. Ryoo, X.J. Chan, T.J. Kim, D.H. Kim, How Pt interacts with  $\text{CeO}_2$  under the reducing and oxidizing environments at elevated temperature: the origin of improved thermal stability of Pt/ $\text{CeO}_2$  compared to  $\text{CeO}_2$ , *J. Phys. Chem. C* 120 (2016) 25870–25879.

[34] Y. Wang, Y.P. Zhai, D. Pierrel, M. Flytzani-Stephanopoulos, Silica-encapsulated platinum catalysts for the low-temperature water-gas shift reaction, *Appl. Catal. B* 127 (2012) 342–350.

[35] Z. Jin, F. Wang, F. Wang, J.X. Wang, J.C. Yu, J.F. Wang, Metal nanocrystal-embedded hollow mesoporous  $\text{TiO}_2$  and  $\text{ZrO}_2$  microspheres prepared with polystyrene nanospheres as carriers and templates, *Adv. Funct. Mater.* 23 (2013) 2137–2144.

[36] C. Galeano, J.C. Meier, M. Soorholtz, H. Bongard, C. Baldizzone, K.J.J. Mayrhofer, F. Schüth, Nitrogen-doped hollow carbon spheres as a support for platinum-based electrocatalysts, *ACS Catal.* 4 (2014) 3856–3868.

[37] L.C. Wang, X.S. Huang, Q. Liu, Y.M. Liu, Y. Cao, H.Y. He, K.N. Fan, J.H. Zhuang, Gold nanoparticles deposited on manganese(III) oxide as novel efficient catalyst for low temperature CO oxidation, *J. Catal.* 259 (2008) 66–74.

[38] X.Y. Li, Y.X. Liu, J.G. Deng, K.F. Zhang, S.H. Xie, X.T. Zhao, J. Yang, H.X. Lin, G.S. Guo, H.X. Dai, Enhanced catalytic performance for methane combustion of 3DOM  $\text{CoFe}_2\text{O}_4$  by co-loading  $\text{MnO}_x$  and Pd–Pt alloy nanoparticles, *Appl. Surf. Sci.* 403 (2017) 590–600.

[39] S. Behar, N.A. Gómez-Mendoza, M.A. Gómez-García, D. Swierczynski, F. Quignard, N. Tanchoux, Study and modelling of kinetics of the oxidation of VOC catalyzed by nanosized Cu–Mn spinels prepared via an alginate route, *Appl. Catal. A* 504 (2015) 203–210.

[40] B. Chen, C. Bai, R. Cook, J. Wright, C. Wang, Gold/cobalt oxide catalysts for oxidative destruction of dichloromethane, *Catal. Today* 30 (1996) 15–20.

[41] S.H. Xie, Y.X. Liu, J.G. Deng, J. Yang, X.T. Zhao, Z. Han, K.F. Zhang, Y. Wang, H. Arandiyani, H.X. Dai, Mesoporous CoO-supported palladium nanocatalysts with high performance for *o*-xylene combustion, *Catal. Sci. Technol.* 8 (2018) 806–816.

[42] L.F. Liotta, M. Ousmane, G.D. Carlo, G. Pantaleo, G. Deganello, A. Boreave, A. Giroir-Fendler, Catalytic removal of toluene over  $\text{Co}_3\text{O}_4$ – $\text{CeO}_2$  mixed oxide catalysts: comparison with Pt/ $\text{Al}_2\text{O}_3$ , *Catal. Lett.* 127 (2009) 270–276.

[43] X. Chen, X. Chen, S.C. Cai, J. Chen, W.J. Xu, H.P. Jia, J. Chen, Catalytic combustion of toluene over mesoporous  $\text{Cr}_2\text{O}_3$ -supported platinum catalysts prepared by in situ pyrolysis of MOFs, *Chem. Eng. J.* 334 (2018) 768–779.

[44] J.Y. Zhang, C. Rao, H.G. Peng, C. Peng, L. Zhang, X.L. Xu, W.M. Liu, Z. Wang, N. Zhang, X. Wang, Enhanced toluene combustion performance over Pt loaded hierarchical porous MOR zeolite, *Chem. Eng. J.* 334 (2018) 10–18.

[45] S. Zhao, K. Li, S. Jiang, J.H. Li, Pd–Co based spinel oxides derived from pd nanoparticles immobilized on layered double hydroxides for toluene combustion, *Appl. Catal. B* 181 (2016) 236–248.

[46] S. Zhao, F.Y. Hu, J.H. Li, Hierarchical core-shell  $\text{Al}_2\text{O}_3$ @Pd–CoAlO microspheres for low-temperature toluene combustion, *ACS Catal.* 6 (2016) 3433–3441.

[47] Y.N. Liao, X.N. Zhang, R.S. Peng, M.Q. Zhao, D.Q. Ye, Catalytic properties of manganese oxide polyhedra with hollow and solid morphologies in toluene removal, *Appl. Surf. Sci.* 405 (2017) 20–28.

[48] J. Li, H. Na, X. Zeng, T. Zhu, Z. Liu, In situ DRIFTS investigation for the oxidation of toluene by ozone over Mn/HZSM-5, Ag/HZSM-5 and Mn–Ag/HZSM-5 catalysts, *Appl. Surf. Sci.* 311 (2014) 690–696.

[49] F. Rainone, D.A. Bulushev, L. Kiwi-Minsker, A. Renken, DRIFTS and transient-response study of vanadia/titania catalysts during toluene partial oxidation, *Phys. Chem. Chem. Phys.* 5 (2003) 4445–4449.